Anchoring of turbulent premixed hydrogen/air flames at externally heated walls

Sebastian Klukas [a],[*], Marcus Giglmaier [a], Nikolaus A. Adams [a], Moritz Sieber [b], Sebastian Schimek [b], Christian Oliver Paschereit [b]

[a] Chair of Aerodynamics and Fluid Mechanics, Technical University of Munich, Boltzmannstr. 15, Garching bei München, 85748, Germany
[b] Chair of Fluid Dynamics, Technische Universität Berlin, Müller-Breslau-Str. 8, Berlin, 10623, Germany

HIGHLIGHTS

- Novel test burner design to investigate flame anchoring at heated wall segments.
- Identification of suitable hydrogen/air chemical mechanisms and turbulence models.
- Successful experimental validation for various operating conditions.
- Limits to universal applicability of eddy dissipation concept parameters identified.

ARTICLE INFO

ABSTRACT

A joint experimental and numerical investigation of turbulent flame anchoring at externally heated walls is presented. The phenomenon has primarily been studied for laminar flames and micro-combustion while this study focuses on large-scale applications and elevated Reynolds number flows. Therefore, a novel burner design is developed and examined for a diverse set of operating conditions. Hydroxyl radical chemiluminescence measurements are employed to validate the numerical method. The numerical investigation evaluates the performance of various hydrogen/air kinetics, Reynolds-averaged turbulence models and the eddy dissipation concept (EDC) as a turbulence-chemistry interaction model. Simulation results show minor differences between detailed chemical mechanisms but pronounced deviations for a reduced kinetic. The baseline k-ω turbulence model is assessed to most accurately predict flame front position and shape. Universal applicability of EDC modeling constants is contradicted. Conclusively, the flame anchoring concept is considered a promising approach for pilot flames in continuous combustion devices.

Please cite this article as: Klukas S et al., Anchoring of turbulent premixed hydrogen/air flames at externally heated walls, International Journal of Hydrogen Energy, https://doi.org/10.1016/j.ijhydene.2020.08.201

Introduction

Controlled flame anchoring is a regular prerequisite for continuous combustion devices. Exemplary applications range from micro-combustors over jet engines to scramjets [1–9]. In general, steady anchoring of flames may be realized by three different approaches: flow recirculation, supersonic shocks or heat transfer. Recirculation-based flame holding is induced either by wall cavities [4–6], bluff bodies [1,7,8] or swirl [9]. Cavities and bluff bodies are geometry modifications which come in various shapes and forms, whereas swirl stabilized combustion makes use of a hydrodynamic induced recirculation in strongly swirling jets. Shock-induced combustion applications utilize the enhanced thermodynamic state behind a shock wave to continuously ignite a mixture [10–12]. Additionally, heat abduction, for example in form of porous media [13], or heat introduction by external means may lead to flame anchoring. While the latter concept has been comprehensively studied for laminar flames and micro-combustion [6,8,14–20], it is relatively unexplored for turbulent flames in the macroscopic scale. This study aims to investigate the phenomenon thoroughly by numerical and experimental analysis. Therefore, successful validation of the implemented numerical method and apprehension of the impact of major modeling parameters are primary objectives. An additional prospective outcome of the presented work are first insights into the adaptability of the investigated flame anchoring mechanism to pilot flames in large-scale dual-fuel nanoparticle production burners using flame spray pyrolysis.

Flame stabilization by supplementary heat introduction is categorized as excess enthalpy combustion [21]. It describes the behavior of a flamelet in a continuously perfused duct or pipe and especially its thermal interplay with adjacent walls. In this configuration excess heat of the burnt gas is conducted through the neighboring wall to the unburnt upstream mixture, thereby heating it up and extending its flamability limits. The detailed behavior depends on the heat transfer coefficient between fluid and solid, heat conduction capability of the wall as well as its thermal heat capacity. Without any external wall heating, the flame front tends to advance back and forth as well as to extinguish and reignite periodically [15]. To remedy this issue, additional external heat is introduced into a specified wall segment. This leads to a less sensitive flame-wall interaction and allows for spatial control of the flame front position. The general effect has been studied with a particular focus on laminar flames [15,16].

To create a well-defined test case, a novel burner design is developed and examined thoroughly. It features an elevated turbulence degree inferring highly non-uniform local flame speeds which makes quasi-steady flame anchoring challenging. This obstacle can be overcome by the employed flame anchoring mechanism. Precise numerical analysis of the devised burner requires correct treatment of turbulent flame front behavior, which is determined by the interplay of turbulence, reaction pace and wall quenching. While focusing on the Reynolds-averaged Navier-Stokes (RANS) equations in axisymmetric domains, the interaction of turbulence and chemistry is prioritized by evaluating species reaction source terms with the well-established eddy dissipation concept.

One of the benefits of excess enthalpy flame holders is that very lean but stable burning conditions are attainable. Hence, their potential for ultra-lean combustion is evaluated. Low equivalence ratios reduce turbulent flame speeds and allow for moderate flow velocities as well as bulk Reynolds numbers. In addition, they lead to weakened NO_x production and flame temperatures benefiting corrosion behavior as well as environmental concerns. Hydrogen fuel in combination with air as an oxidizer is employed. While being one of the most interesting fuels for future clean energy solutions, hydrogen combustion comprises very high flame speeds and thus opposes the acknowledged benefits of extremely lean combustion. Therefore, the experimental burner features elevated Reynolds numbers while operating ultra-lean air-fuel ratios.

After presenting the burner setup and its operating conditions, the paper is structured as follows. First, a review of the applied numerical method and especially the EDC is exercised. Secondly, different kinetic mechanisms for hydrogen/air combustion are examined and compared with respect to their ability to portray heat losses as induced by adjacent walls. Thirdly, the influence of various turbulence models and EDC modeling parameters on flame shape and simulation results in general are discussed. Finally, operating conditions reflecting the impact of equivalence ratio, bulk Reynolds number as well as unburnt mixture temperature are reviewed and utilized for experimental validation of the numerical results.

Experimental setup

To investigate anchoring of turbulent flames at preheated walls, a novel burner design is implemented and tested thoroughly. The device is constructed to operate under a wide range of equivalence ratios, inlet mass flow rates and unburnt mixture temperatures. The detailed experimental setup, employed measurement techniques and operating conditions are described in this section.

Burner design and instrumentation

As displayed in Fig. 1 the burner assembly features the following sections with their respective function:

a) An electric preheater provides hot air at a pressure of up to 6 bar and an adjustable temperature between 473 K and 673 K.
b) The flow is decelerated through a divergent nozzle before a
c) set of perforated plates is passed to diminish turbulent fluctuations and obtain a homogeneous velocity across the section.
d) After the straightened flow reaccelerates in a converging nozzle, hydrogen fuel is injected radially through six injection ports, equally spaced in circumferential direction.
e) Downstream, a long steel tube ensures that fuel and oxidizer have sufficient time to fully mix, which justifies the assumption of a premixed flame. Full mixing was confirmed by non-reactive three-dimensional CFD simulations.
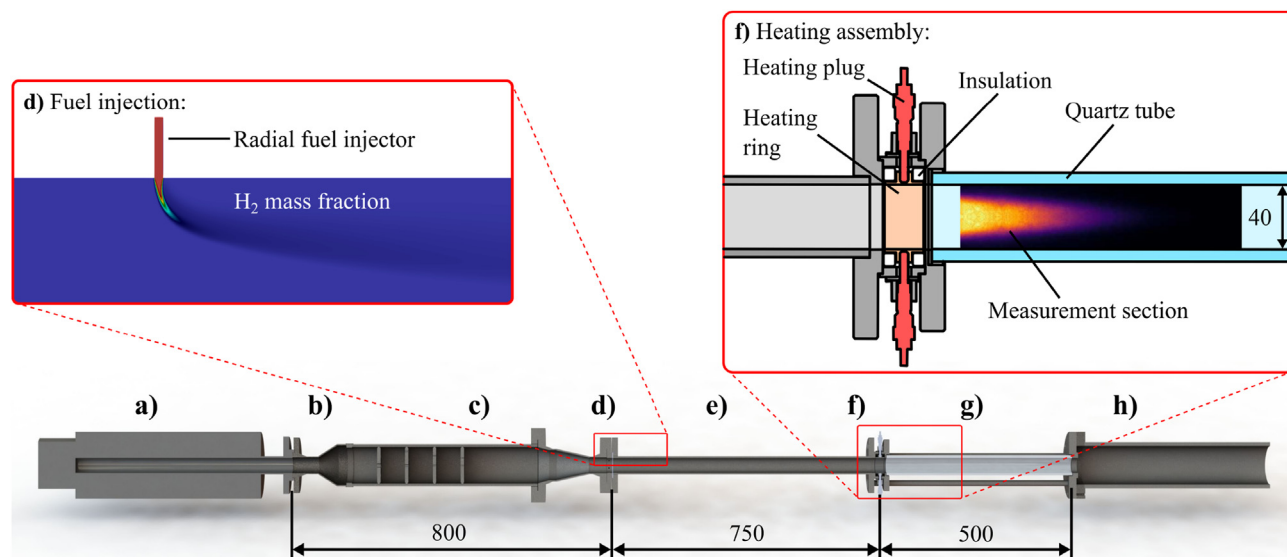
Fig. 1 – Schematic of the experimental burner setup. Details of the heating assembly and fuel injection are visualized in separate magnified areas.

f) The heating assembly, which functions as a flame holder, is located at the very end of the steel tubing and provides the necessary means for external heating of a separate wall section. This eventually leads to continuous ignition.

g) A quartz glass tube makes the flame front visually accessible to the measuring equipment.

h) Finally, a water cooled exhaust pipe is utilized to chill down the hot reaction products before they are released into the environment.

The heating assembly comprises four electric heating plugs connected to a heating ring as well as insulation bands (top right of Fig. 1). Therefore, the heating ring partially replaces the chamber wall while insulation inhibits heat conduction to adjacent parts. Equal spacing of the heating plugs ensures a uniform temperature distribution within the ring and thus symmetrical flame positioning. In that way, a distinctive locally heated wall is devised. The design is optimized to avoid any wall gaps in order to diminish disturbance of the turbulent boundary layer.

The total axial dimension of the burner, excluding preheater and exhaust, is 2.05 m and the respective wall thicknesses of steel tube and glass pipe are 5 mm and 7.5 mm. Metal parts upstream of the heating assembly are thermally isolated with stone wool. Temperature measurements within the burner confirm that no significant wall heat loss takes place where the isolation is applied. The installed heating ring extends for 24 mm and is placed 20 mm in front of the glass tube.

The measurement setup provides the means for a qualitative comparison between numerics and experiment. For this purpose relevant boundary conditions as well as the flame's reaction zone are quantified and evaluated. Air and hydrogen inlet mass flow rates are registered by Coriolis mass flow meters. Temperature measurements of the mixture are obtained by thermocouples placed along the burner's axis. The heating ring is equipped with additional thermocouples to determine the local wall temperature. Equal temperature

distribution inside the ring is confirmed visually. To assess general flame shape and quantify the position of the reaction front, a CCD camera with image intensifier is utilized. By appliance of an optical filter transmitting a wavelength of 308 nm the hydroxyl radical (OH*) distribution becomes discernible. The intensifier is operated with an exposure time of 200 μs while the flame shape is obtained from an average of 1500 images acquired at a rate of 5 Hz as three sets of 500 images.

Operating conditions

The influence of three major reactive flow characteristics and their effect on burner stability and overall flame shape is investigated: equivalence ratio, inlet mass flow rate and unburnt mixture temperature, which is primarily determined by the hot air temperature. The inlet mass flow rate mainly influences the bulk Reynolds number. The experimental setup described above allows precise tuning of these variables. To illustrate their respective influence, six operating points are considered as displayed in Table 1.

Turbulent premixed combustion is categorized by its flame front behavior, specifically by the reaction's interaction with

Table 1 – Featured operating conditions determined by the mixture's total mass flow rate $\dot{m}_{total}$, the injected air temperature T_{air}, equivalence ratio Φ, bulk Reynolds number Re, turbulent Reynolds number Re_t as well as turbulent Damköhler number Da_t.

Case	$\dot{m}_{total}$ $\left[\text{kg h}^{-1}\right]$	T_{air} [K]	Φ [−]	Re [−]	Re_t [−]	Da_t [−]
1	80.47	673	0.2	21,463	69.1	1752
2	80.67	673	0.3	21,555	69.4	1745
3	60.5	673	0.3	17,137	56.7	2228
4	60.35	673	0.2	16,096	53.7	2254
5	80.47	573	0.3	23,971	76.1	2710
6	80.47	473	0.3	27,338	85.4	4610

turbulence [22,23]. Based on turbulent Reynolds number Re_t and turbulent Damköhler number Da_t various premixed combustion regimes are characterized. For the defined operating conditions the burner's combustion behavior is placed in the quasi-steady corrugated flamelets regime ($Da_t \gg 1$ and $Re_t \gg 1$). In this area turbulence-chemistry interaction mandates to be taken into account for all numerical calculations.

Numerical setup and theory

To investigate numerically the presented flame-anchoring mechanism, the fully compressible Reynolds-averaged Navier-Stokes (RANS) equations are solved by the commercial CFD code Ansys Fluent in version 2019 R3 [24]. One of the challenges inherent to turbulent time-averaged combustion calculations is the determination of each species reaction rate. Since turbulence driven mixing processes strongly affect these rates, the eddy dissipation concept is utilized as a modeling approach to evaluate reaction source terms. Besides a description of the general numerical setup, this combustion model is briefly reviewed in the following.

Numerical setup

To achieve a steady-state solution, a fully-coupled implicit solution procedure utilizing an algebraic multigrid pressure-based finite volume solver, is applied. A pseudo-transient implicit under-relaxation formulation is employed for a stable and efficient convergence behavior. Spatial discretization is usually performed by the quadratic interpolation upwind (QUICK) scheme ensuring second order accuracy [25]. Only the pressure equation is discretized by the second order PRESTO! scheme. The closure problem of the time-averaged Navier-Stokes equations is addressed by established ω-based eddy viscosity as well as Reynolds stress turbulence models. A detailed description is omitted at this point but has been addressed at length by Ref. [26–28].

Although buoyancy may impact the shape of wall anchoring flames [29], gravity effects are assumed negligible. This deduces the assumption of axisymmetric flow conditions, which is confirmed by OH* chemiluminescence measurements during the experimental test campaign. Since heat conduction in the burner's walls plays a major role in the flame anchoring mechanism [16], they are taken into account in the simulations by solving Fourier's heat conduction equation. Thermochemical fluid properties are evaluated by the CHEMKIN software libraries [30]. Therefore, heat capacity is assessed by a fourth order polynomial fit while heat conductivity, viscosity, molecular as well as thermal diffusion coefficients are derived from kinetic theory. Mixture averaging is performed for all transport properties except species diffusion. Bruno et al. [31] concluded that multicomponent diffusion plays an essential factor in turbulent reactive flows. Especially for hydrogen/air mixtures and their inherently high diffusion coefficient of hydrogen species, the overall flow field may be crucially impacted by differential diffusion [32]. Therefore, binary diffusion coefficients are calculated by the Dixon-Lewis method and adapted into the flow by the Maxwell-Stefan diffusion equation. While fluid properties

strongly depend on local flow state, solid material attributes are assumed to be constant and are summarized in Table 2.

Radiation phenomena play a crucial role in the analysis of high temperature reactive flows. Therefore, the discrete ordinates radiation model is applied in the presented configuration. The number of solved transport equations for radiation intensity depends on angular discretization, which in our case comprises 24 control directions. The radiation energy transfer equations are solved in a sequential manner. All surfaces are considered to be grey walls. Special attention is required for the semi-transparent quartz-glass which is the only non-opaque surface in the domain. Therefore, radiation has to be treated as a volumetric and not a pure surface phenomenon. In general, radiation is deemed to be partially diffusive and partially specular. Employed internal emissivities ε and diffusive fractions f_d are listed in Table 2.

The computational domain extends from the radial hydrogen injection until the end of the glass tube. Preceding cold gas mixing simulations including radial fuel injection in a jet in crossflow configuration were conducted. They showed that the reactants are mixed adequately in front of the heated wall segment by depicting an insignificant radial fuel mass fraction gradient at that axial position. Therefore, radial fuel injection is not reflected in all successive reactive flow simulations. Instead, the mixture is assumed to be perfectly premixed at the domain inlet. By considering a long inlet in front of the flame holder, it is ensured that profiles of velocity, turbulent kinetic energy and its dissipation rate are fully developed prior to ignition. Since the fluid temperature upstream of the flame holder remains constant, corresponding Dirichlet boundary conditions are applied (Fig. 2).

To reflect the wall anchoring mechanism correctly, the heating ring is considered as an adjacent wall. Isolation bands, which inhibit heat transfer to neighboring walls, are approximated by adiabatic boundary conditions and missing wall connections. As a necessary simplification all other parts of the heating assembly are neglected. Thus, the impact of the heating plugs is reproduced by applying constant temperature boundary conditions at the borders of the adapted heating ring (Fig. 2). The corresponding hot wall temperature is adjusted such that the maximum temperature within the numerical heating ring conforms to its measured counterpart. At solid wall boundaries to the environment radiative as well as convective external heat transfer conditions are applied. While the total mass flow rate from Table 1 is imprinted at inlet, a constant pressure of 1 bar is applied at the outlet.

To mirror the experimental configuration as accurately as possible, a short steel wall section is placed right before the quartz glass tube. Since hydrogen fuel is injected at room temperature, the applied inlet temperature T_{inlet}, which is equal to the constant wall temperature upstream of the heated wall $T_{w,inlet} = T_{inlet}$, is slightly lower than the reported

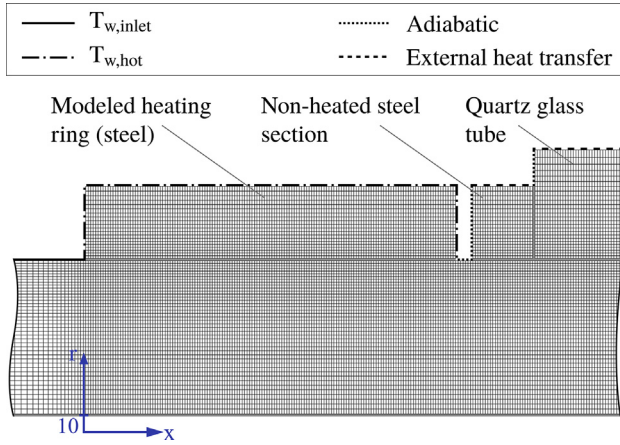| Table 2 — Applied solid material and radiation properties.				
	ρ	c_p	λ	ε	f_d
	[kg m^{-1}]	[J kg^{-1} K^{-1}]	[W m^{-1} K^{-1}]	[–]	[–]
Stainless steel	7900	750	25	0.8	0.5
Quartz glass	2200	740	1.38	0.8	0.1

Fig. 2 — Grid design and implemented thermal boundary conditions. In radial direction only a segment with r ≥ 10 mm is displayed. For enhanced clarity the cell density is reduced by a factor of four.

hot air values in Table 1. Implemented thermal boundary conditions as well as hydrogen mass fractions at inlet are reported in Table 3. To simplify comparison between experimental and numerical data, the axial point of origin ($x = 0$) is placed right at the beginning of the heated wall segment.

The block structured hexahedral mesh is designed around two objectives: First and foremost the condition $y^+ \lesssim 1$ has to be maintained to correctly resolve the turbulent wall boundary layer for all operating conditions. Secondly, the mesh resolution must be fine enough to reflect the thin reaction zone and its quickly recombining intermediate species. To satisfy those requirements, wall adjacent cells feature a radial extend of 40 μm and unity aspect ratio. While the aspect ratio is kept constant along the externally heated section, cells grow exponentially in all axial and radial directions. In total, the grid comprises $1.49 \cdot 10^6$ cells.

Eddy dissipation concept

A critical challenge in turbulent RANS combustion simulations poses the correct treatment of each species' mean reaction rate. Since an evaluation utilizing the Arrhenius approach combined with mean flow quantities leads to significant deviations, a modeling strategy to incorporate turbulence-chemistry interaction has to be applied [23]. One appropriate model applicable to turbulent premixed flames is the eddy dissipation concept (EDC) by Magnussen [33–35]. It is based on the analysis of turbulent scales in the energy cascade and may include arbitrarily complex reaction mechanisms. An extensive review comprising recent developments is

available in Ref. [36] and recapitulated synoptically in this section.

In general and as basis for the EDC, the energy cascade hypothesis assumes that mechanical energy is continuously transferred from the mean flow to the largest eddies, which subsequently pass it on to progressively finer eddies. Viscous dissipation mostly takes place within the smallest eddies, which are also related to the Kolmogorov scales [26]. These scales are furthermore associated to chemical reaction processes since they represent perfectly mixed species at a molecular level, a necessary condition for reaction processes. To transfer these presumptions into a numerical model, each computational cell is divided into a fine structure part of Kolmogorov scale size and a secondary segment representing the surrounding fluid. Consequently, each cell comprises a reacting (fine structures) and a non-reacting part (surrounding fluid).

Typical length and velocity scales are assigned to the fine structure region and are denoted by L^* and u^*, which by definition are of the same order of magnitude as the Kolmogorov scales [37]. When setting the characteristic scales of the fine structures in relation to turbulent flow scales, the fine structure length fraction γ_L is defined as

$$\gamma_L = \frac{u^*}{u'} = \left(\frac{3C_{D2}}{4C_{D1}^2}\right)^{1/4} \left(\frac{\nu \varepsilon}{k^2}\right)^{1/4} \approx \frac{L^*}{L'}. \tag{1}$$

C_{D1} and C_{D2} are constants related to strain rate and energy transfer in the cascade model and designated to represent as many flow regimes as possible. For simplification, a directly proportional EDC modeling constant C_γ as well as the turbulent Reynolds number Re_t are introduced by Magnussen:

$$\gamma_L = C_\gamma \left(\frac{\nu \varepsilon}{k^2}\right)^{1/4} = C_\gamma \, \mathrm{Re}_t^{-1/4} \tag{2}$$

Since the mass share of the fine structure region is given by $\gamma^* = \gamma_L^3$ [34], the mass transfer rate $\dot{m}^*$ between fine structures and their surrounding fluid, in relation to the fine structure mass, is expressed by

$$\dot{m}^* = 2\frac{u^*}{L^*} = \left(\frac{3}{C_{D2}}\right)^{1/2} \left(\frac{\varepsilon}{\nu}\right)^{1/2}. \tag{3}$$

Therefore, the characteristic time scale of fine structures is given by

$$\tau^* = \frac{1}{\dot{m}^*} = \left(\frac{C_{D2}}{3}\right)^2 \left(\frac{\nu}{\varepsilon}\right)^{1/2}, \tag{4}$$

which again may be rewritten in terms of a linear constant C_τ and turbulent Reynolds number

$$\tau^* = C_\tau \left(\frac{\varepsilon}{\nu}\right)^{1/2} = C_\tau \, \mathrm{Re}_t^{-1/2} \frac{k}{\varepsilon}. \tag{5}$$

Default values of the EDC constants equal $C_\gamma = 2.1366$ and $C_\tau = 0.4082$. Since the mass transfer rate in relation to total mass $\dot{m}$ represents the mean rate of molecular mixing [37], it is of higher significance for determination of the reaction source terms. It is derived as

$$\dot{m} = \dot{m}^* \gamma^* = \frac{\gamma_L^2}{\tau^*}. \tag{6}$$

Table 3 — Applied thermal boundary conditions as well as inlet fuel mass fractions.						
Case:	1	2	3	4	5	6
$T_{w,\,inlet}$ [K]	651	639	633	643	558	466
$T_{w,\,hot}$ [K]	1053	1038	1038	1053	1038	1038
$Y_{H_2} \cdot 10^{-3}$ [—]	5.841	8.305	8.264	5.8	5.841	5.841

Here, the modified conversion ratio $\gamma^* = \gamma_L^2$ is utilized to include mixing effects within the fine structure region [35]. Mean fluid quantities are expressed by linear combination

$$\overline{\Psi} = \Psi^0 \left(1 - \gamma_L^3\right) + \Psi^* \gamma_L^3, \tag{7}$$

where superscript 0 denotes properties of the surrounding fluid in each cell. Utilizing this formulation species mass fractions are expressed by

$$Y_i^0 = \frac{\overline{Y_i} - Y_i^* \gamma_L^3}{1 - \gamma_L^3}. \tag{8}$$

When Y_i^* corresponds to species mass fractions in the fine structure region after numerical integration of all chemical reactions, the individual reaction of each specie is expressed as

$$\overline{\omega_i} = \overline{\rho}\, \dot{m}\, \chi (Y_i^* - Y_i^0). \tag{9}$$

While χ denotes the fraction of fine structures that actually participate in the reaction and is usually assumed to be unity. Substitution of equations (6) and (8) yields the reaction rate depending on mean quantities:

$$\overline{\omega_i} = \overline{\rho}\, \frac{\gamma_L^2}{\tau^*(1 - \gamma_L^3)} (Y_i^* - \overline{Y_i}) \tag{10}$$

The computationally most expensive task of reactive flow simulations is numerical integration of chemical kinetics. To improve this limitation, the reacting fine structure region is solved by a zero-dimensional model. Originally, a perfectly stirred reactor (PSR) was proposed for this purpose [33]. It features an isothermal and isobaric set of ordinary differential equations (ODE) which is solved to steady-state. Due to the persisting extensive numerical cost of this operation, the selected solver follows a different approach by neglecting mixing between fine structures and surrounding fluid to form a simplified set of ODEs referred to as a plug flow reactor (PFR) [36]. Instead of finding a steady state solution, the PFR ODE system is only integrated for the fine structure time scale τ^*. Boesenhofer et al. [36] pointed out that there are only minor differences in accuracy between the two concepts.

Two limiting scenarios have to be considered when looking at wall bounded flows in combination with the EDC combustion model. Since turbulent kinetic energy approaches zero at walls, γ_L advances towards infinity which has to be omitted. An elegant solution to eliminate this behavior is to apply blending functions for γ_L depending on Re_t [38]. A more straightforward approach is to apply a limiter directly onto γ_L, which performs comparably well and is thus employed [38]. A second singularity similar to the first one is encountered when γ_L approaches unity. This corresponds to cells entirely filled by fine structures and a species reaction rate approaching infinity. De et al. [39] introduced the analogy that the EDC changes the mean species mass fraction by linear relaxation, thus avoiding the complex nonlinear problem. In this context the relation of the linear mixing problem's timescale is described as

$$\frac{\tau^*}{\tau_{mix}} = \frac{\gamma_L^2}{1 - \gamma_L^3} < 1. \tag{11}$$

Therefore, the stability condition and limiting value for the fine structure mass fraction, which requires the reaction time τ^* to be smaller than the mixing time scale τ_{mix}, equals $\gamma_L < 0.755$.

As the flame-wall interaction mode of the configuration is sidewall quenching (SWQ), reactions right at the wall have to be suppressed to properly reflect physical quenching of the flame. Since the EDC model is inhibited in its ability to account for this effect and instead assigns the described limiter, wall adjacent reactions are prevented by setting the reaction source terms to zero in all wall neighboring cells. Although default EDC modeling constants perform well for a broad application range, they are modified to fit the operating conditions of the featured reactive flow more accurately. Depending on the general flow configuration multiple variations of EDC modeling parameters C_γ and C_τ have been reported [39–43]. In the present setup default EDC modeling constants overpredict flame length. Therefore, an increase of the absolute value of species reaction source terms is necessary to fit the experimental values. This is achieved by employing $C_\gamma = 3.0$ as an adapted EDC modeling parameter. The same value is reported in Ref. [39]. A more detailed assessment of EDC modeling constants is given in section Experimental validation.

Chemical reaction kinetics evaluation

Before conducting a detailed numerical investigation featuring finite rate chemistry, a review of available reaction mechanisms is worthwhile. For that purpose, chemical kinetics are evaluated in a simplified canonical configuration reflecting a steady one-dimensional premixed flame. To ensure that each mechanism is able to reproduce the central physical phenomenon, it has to be part of the canonical problem as well [16]. In the presented setup flame shape, position and extinction behavior are particularly determined by heat transfer processes at the wall. Therefore, the evaluation of reaction mechanisms includes non-adiabatic premixed flame calculations under heat loss conditions. Although hydrogen/air kinetics have been explored for a number of different applications [44–46], this study distinctly focuses on the influence of heat loss and derived quenching behavior.

For comparison five reaction mechanisms are taken into account. Four of them are considered detailed (Konnov [47], Li [48], UCSD [49], USC [50]) while the final one is reduced (Boivin [51]). They collectively feature four identical major species (H_2, O_2, N_2, H_2O) as well as five minor ones (OH, H_2O_2, H, O, HO_2). The number of total reactions varies from 12 to 29. While all kinetics incorporate pressure dependent ($N_{Pressure}$) as well as fall-off reactions ($N_{Fall-off}$), only the simplified mechanism comprises irreversible reactions ($N_{Irreversible}$). A more detailed perspective on the different kinetics is summarized in Table 4. Due to their much larger chemical time scale, nitrogen reactions are neglected in all calculations. The experimental setup allows for OH* chemiluminescence measurements. That is why, in addition to hydrogen oxidation, a sub-mechanism for hydroxyl radical reactions has to be included

into the chemical mechanism. For the study at hand the corresponding sub-mechanism of Kathrotia [52] is incorporated.

The simplified numerical formulations are solved by the Cantera laminar reacting flow solver [53]. The initial problem of reduced complexity is an adiabatic one-dimensional freely propagating flame. This configuration is well suited to examine laminar flame speed as an inherent property of reaction kinetics. The influence of equivalence ratio on laminar flame velocity is depicted and compared to its experimental counterpart in Fig. 3. The experimental results are either obtained by constant volume laminar explosion bombs [54–56] or the laminar Bunsen burner method [57]. All simplified calculations are carried out under atmospheric pressure conditions since the impact of pressure variations in the burner setup are considered subordinate. At standard state conditions the deviation between experiment and numerical calculations for all featured mechanisms, lies within the usually reported error margin. The series is repeated for elevated unburnt mixture temperatures to investigate settings closer to the actual operating conditions. As detailed in Fig. 3 there are only minor differences for lean flame fronts ranging from $\Phi = 0.2$ to $\Phi = 0.3$. Over the entire equivalence ratio range the largest disparity is observed between the detailed Konnov and reduced Boivin chemical kinetics.

Since wall heat transfer and subsequent quenching characterize the major physical phenomenon, a canonical configuration incorporating these effects is analyzed. For this purpose the energy equation of the laminar flame solver is altered to incorporate an additional heat sink term. The heat sink is realized by introducing a heat loss factor γ_{loss} to the already implemented heat of reaction source term. Thus, the complete heat of reaction source term in the energy equation of the simplified reactive flow solver is realized as

$$(1 - \gamma_{loss}) \sum_{k}^{n_k} h_k W_k \dot{\omega}_k. \tag{12}$$

While W_k depicts the molar mass of species k, h_k corresponds to its enthalpy and $\dot{\omega}_k$ to its molar production rate. By inclusion of the heat loss factor only the reaction front of the premixed flame is impacted while the remaining flame remains unaltered [58].

Fig. 4 shows the influence of the established heat loss factor on laminar flame velocity as well as hydrogen peroxide concentration as an intermediate species. In general, quenching is observed at an approximate heat loss factor of $\gamma_{loss} = 0.745$. Discrepancies in laminar flame speed between the applied chemical kinetics become smaller as the
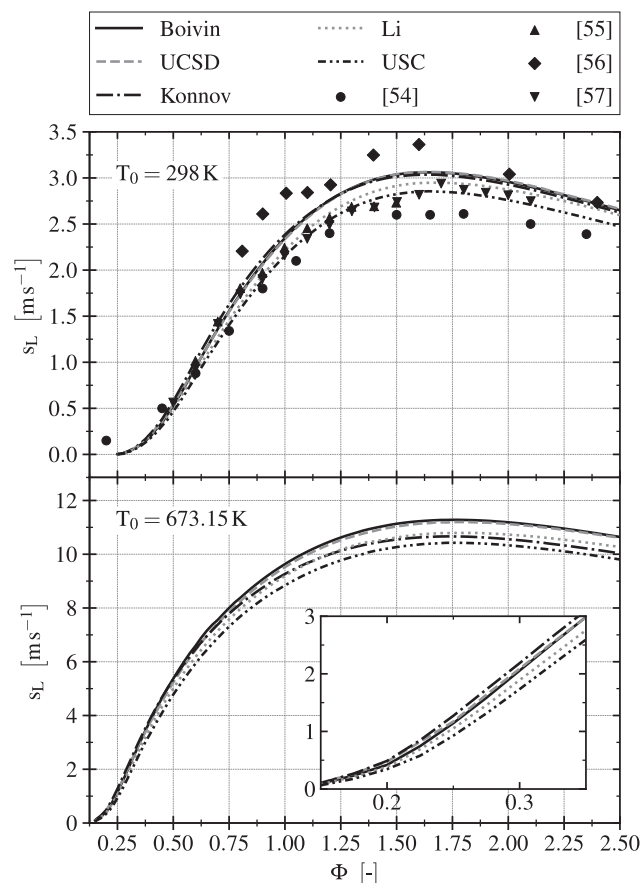
Fig. 3 – Validation of studied chemical kinetics by experimental results. Laminar flame speed (s_L) at different equivalence ratios (Φ) is utilized for comparison. Numerical results for different mechanisms are depicted by lines and obtained by one-dimensional premixed flame calculations. Symbols correspond to experimental data. Top: Unburnt mixture at room temperature for validation. Bottom: Elevated unburnt mixture temperature reflecting actual operating conditions.

extinction point is approached. However, deviations in H_2O_2 mass fraction between detailed and simplified mechanisms intensify for greater heat loss factors. This effect is further investigated in Fig. 5 with help of the non-dimensional variable ξ to simplify visualization of the narrow reaction zone:

$$\xi = \frac{x - x_{ff}}{\Delta_{ff}} \tag{13}$$

Here, x_{ff} and Δ_{ff} denote flame front position and thickness. The position is determined by the maximum location of the heat of reaction while flame thickness is derived from the onset and end of its corresponding distribution. Fig. 5 visualizes minor species H, OH and H_2O_2 under adiabatic and non-adiabatic ($\gamma_{loss} = 0.5$) imposed heat loss conditions. Species plots in Fig. 5a and b show a clear trend of diminished intermediate species concentration under heat loss conditions while all employed reaction kinetics, including the reduced one, behave fairly similar. This again changes for the hydrogen peroxide concentration, where two major observations are

Table 4 – Distribution of reaction types in the investigated hydrogen/air reaction mechanisms. As the hydroxyl radical sub-mechanism is identical in each chemical kinetics, its reactions are not considered here.

	N_{Total}	$N_{Fall-off}$	$N_{Pressure}$	$N_{Irreversible}$
Konnov [47]	29	4	4	0
Li [48]	21	2	4	0
UCSD [49]	23	2	4	0
USC [50]	25	2	4	0
Boivin [51]	12	2	2	6

worked out. First, additional heat loss only slightly alters the maximum H_2O_2 species concentration when any of the detailed kinetics are employed (Fig. 5c). On the other hand, the maximum H_2O_2 mass fraction changes significantly under heat loss conditions for the simplified mechanism. Secondly, this maximum concentration is more than twice as high compared to detailed kinetics. If the trend from Fig. 4 is considered this discrepancy in concentration is expected to further enhance until peak deviation is established at around $\gamma_{loss} = 0.65$.

Although the reduced mechanism of Boivin performs comparably well in adiabatic calculations, it demonstrates discrepancies for minor species under heat loss conditions. Therefore, the computationally more expensive reaction mechanism by Li is selected for the subsequent numerical study. Hence, in addition to the chemiluminescence reactions, ten species and 29 reactions are considered in all consecutive simulations. It should be noted that the other detailed chemical kinetics perform very similar to the Li mechanism while including a higher number of reactions. They are further investigated in section Influence of mesh resolution and chemical kinetics.

Numerical investigation

An examination of numerical aspects of wall anchoring turbulent flames in the featured configuration is presented in the following chapter. It focuses on the influence of mesh resolution, choice of chemical kinetics as well as RANS-based turbulence modeling. Furthermore, a comprehensive review of the general flame structure and flame-wall interaction by SWQ is carried out.

Flame structure and wall anchoring phenomenon

The general flame shape and composition are displayed in Fig. 6 by visualizing flame temperature and species distributions. The major species H_2O, minor species OH as well as the

quickly recombining species H are shown. Applied boundary conditions correspond to the previously defined case 1, which is utilized as a reference case for most of the numerical investigation in this chapter. As the coordinate system corresponds to the one defined in Fig. 2, the flame anchors steadily shortly after the front face of the externally heated wall segment.

As briefly discussed in the introduction, steady flame-wall anchoring is achieved by interaction of reaction products and fresh reactants with adjacent walls. In detail, hot reaction products transfer heat into neighboring walls downstream of the flame front by convection and radiation. In return heat conduction within the solid is induced. This mechanism is responsible for increasing wall temperatures upstream of the flame front, which eventually leads to heat transfer into the fluid right in front of the reaction zone. Therefore, ignition of the unburnt gas is induced continuously. The described phenomenon by itself may already lead to steady flame anchoring. Additional external heating of a secluded wall segment enhances the anchoring process and forces it to take place at a specific wall location by inhibiting flame front propagation. In the described numerical setup this behavior is imposed by application of constant temperature boundary conditions at all heated wall segments (Fig. 2). Thus, heat introduced into the modeled heating ring may only escape back into the fluid or locally increase the wall's temperature.

Fig. 7 displays this behavior by visualizing wall temperature, heat of reaction and velocity streamlines. Due to disparate temperature scales between externally heated and non-heated walls, each wall temperature distribution is normalized separately. Red isolines depict one percent of the maximum heat release rate and therefore correspond to the beginning and end of the reaction zone. Depending on flame temperature, the operating conditions feature measured hot wall temperatures between $T_{w,hot} = 1038\,K$ and $T_{w,hot} = 1053\,K$ (Table 3). As the flame anchoring position of case 1 is very similar in most considered operating conditions, two more extreme hot wall conditions are investigated. These correspond to an imprinted hot wall temperature of $T_{w,hot} = 1270\,K$ (Fig. 7 top) and $T_{w,hot} = 1020\,K$ (Fig. 7 bottom).

From the displayed results it is inferred that the unburnt mixture is ignited immediately at the beginning of the heated segment if excessive wall temperatures are present. Under these conditions additional heat conduction through the wall, induced by hot reaction products, is expendable. Nonetheless, elevated wall temperatures still expand the reaction's flammability limits and lead to more reliable flame anchoring. As expected, an opposite trend is observed for a decrease in heated wall temperature. Here, a stable flame anchoring position is achieved further downstream compared to case 1. Thus, if the actual hot wall temperature of case 1 is applied, the flame anchors in between these two more extreme positions. In general, the flame anchoring position is more sensitive to changes of external heating means in the lower end of the applied hot wall temperature spectrum. Although the influence of external heating on the flame anchoring position is apparent, it has no significant impact on flame shape and overall flame composition. A general requirement for the presented flame anchoring technique is that the absolute
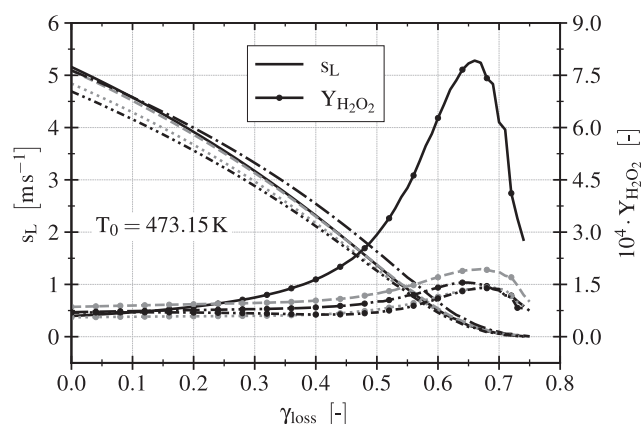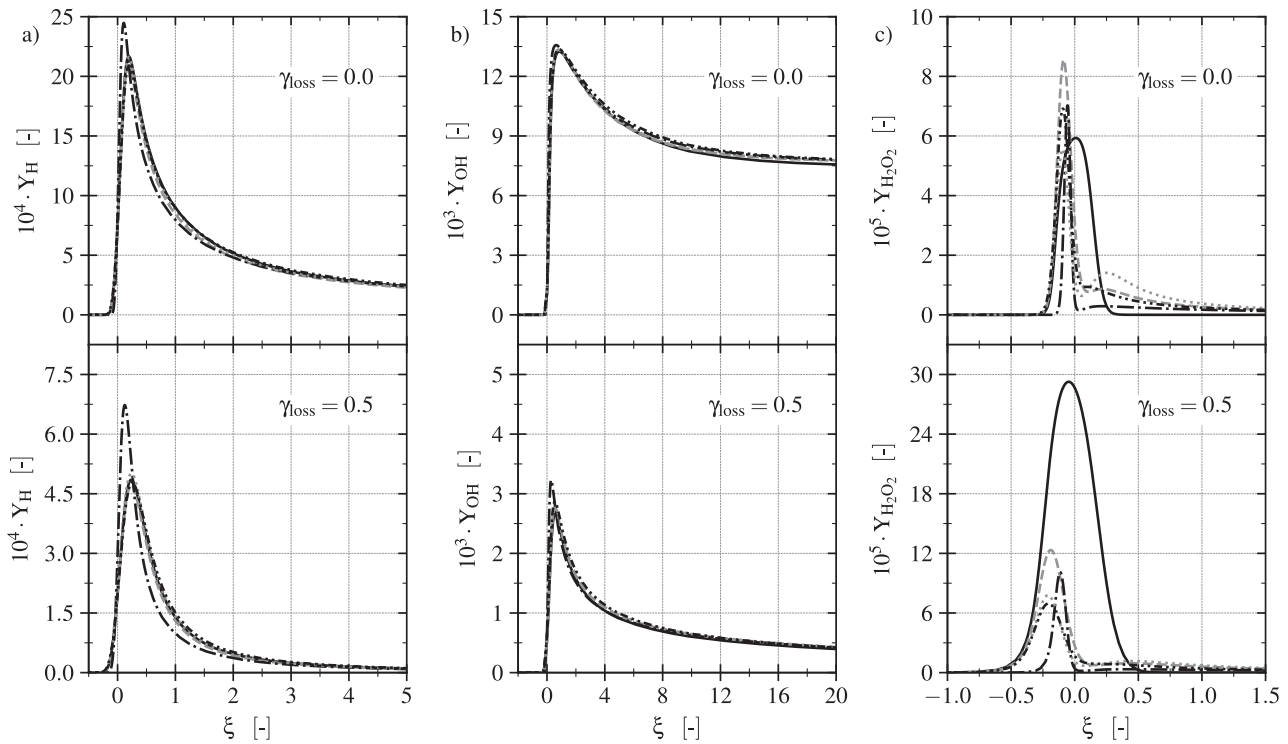

Fig. 4 – Investigation of extinction behavior by application of an additional heat loss factor. Different mechanical mechanisms are examined and depicted by lines. For line style definitions see Fig. 3. Laminar flame speed and hydrogen peroxide mass fraction are plotted over the heat loss factor.

Fig. 5 – Influence of chemical kinetics on intermediate species mass fractions under adiabatic (top row: $\gamma_{loss} = 0$) and non-adiabatic (bottom row: $\gamma_{loss} = 0.5$) conditions. a) Hydrogen atom, b) Hydroxyl, c) Hydrogen peroxide concentrations are plotted over non-dimensional variable ξ. Lines depict applied mechanisms. For line style definitions see Fig. 3. The distribution of the quickly recombining H_2O_2 molecule displays pronounced deviations for the simplified mechanism under heat loss conditions. Here, the maximum concentration is more than twice as high as for comparable detailed kinetics.
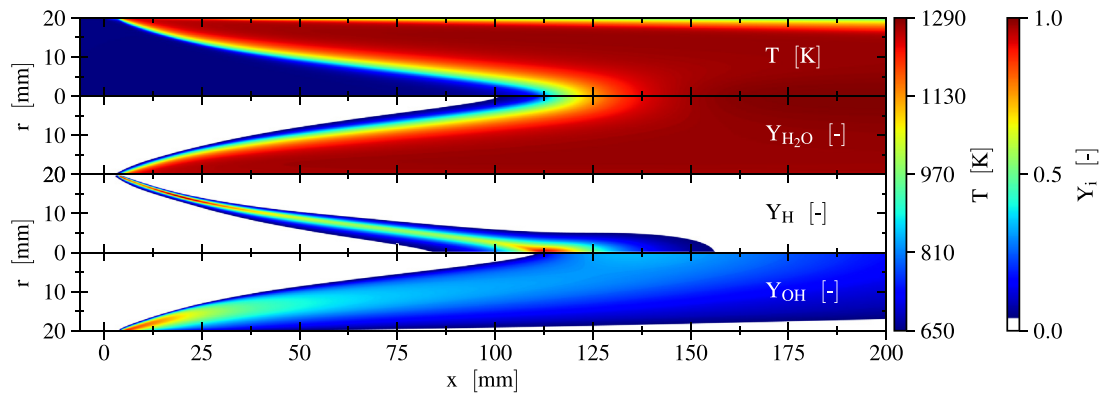
Fig. 6 – General flame structure of the investigated configuration. Contour plots of temperature, water, hydrogen atom and hydroxyl mass fractions are visualized. Mass fractions below five percent are not shown for clarity. The employed operating conditions reflect case 1 while the k-ω BSL turbulence model is employed.

magnitudes of turbulent flame speed and flow velocity match each other reasonably well.

Influence of mesh resolution and chemical kinetics

To verify the implemented numerical setup, a mesh study featuring a refined grid is conducted. For the fine mesh the resolution is doubled compared to the original grid. This leads to a minimum wall adjacent cell size of 20 µm and a total cell count of $5.96 \cdot 10^6$ quadrangular cells. As depicted in Fig. 8 the finer mesh does not lead to significant deviations in flame shape or anchoring position. Thus, the coarser mesh is considered adequate to reflect all relevant physical phenomena. As grid independence is shown exemplarily for the Li mechanism, the examination is not repeated for another chemical kinetic.

Since the preceding examination of chemical kinetics is performed for one-dimensional canonical problems, the
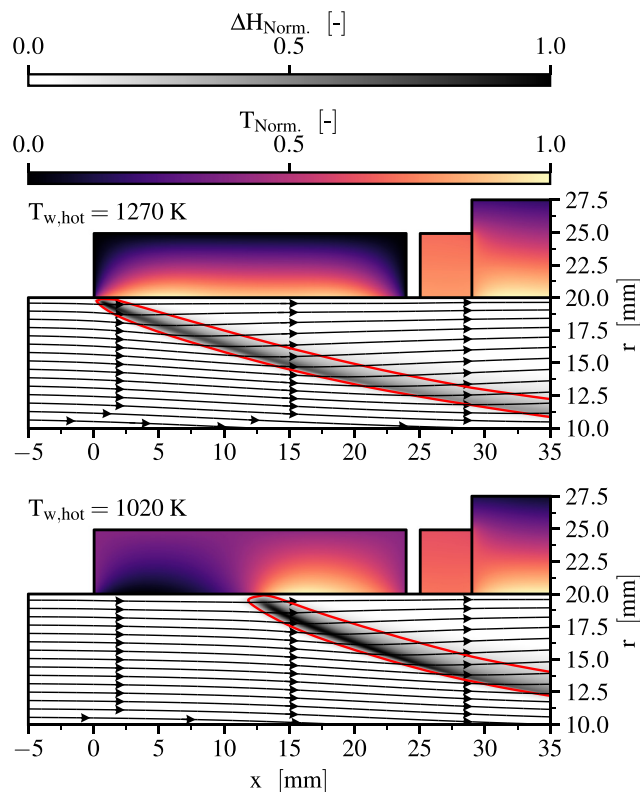
Fig. 7 − Influence of hot wall temperature on flame-wall interaction and anchoring position. Steady flame anchoring is visualized for $T_{w,hot} = 1270$ K (top) and $T_{w,hot} = 1020$ K (bottom). Otherwise, applied boundary conditions reflect those of case 1 while the k-ω BSL turbulence model is employed. The velocity field is plotted by streamlines while red isolines replicate one percent of the normalized heat release rate $\Delta H_{Norm.}$ distribution. Solid temperature contours are normalized separately for the heated and non-heated wall segments.

already observed in Fig. 3, is also discernible in two-dimensional axisymmetric simulations. But, as both mechanisms lie within the experimentally observed flame speeds (Fig. 3), the much more efficient mechanism by Li is still considered suitable.

RANS-based turbulence modeling

To solve the closure problem of time-averaged Navier-Stokes equations, multiple RANS turbulence models are applied to operational conditions resembling case 1. A detailed performance evaluation is given in the following.

Two-equation turbulence models have already been successfully applied in RANS simulations of premixed combustion [5,17,19,20]. This work aims to extend the assessment of turbulence models interacting with the EDC for wall anchoring flames under SWQ conditions. Due to their inherent ability to resolve turbulent boundary layers, ω-based models are exclusively adopted for the study at hand. For this purpose the standard (STD), baseline (BSL) and shear stress transport (SST) k-ω models are selected as classical two-equation models. In addition, an ω-based Reynolds stress turbulence model featuring five transport equations is evaluated as well. In conclusion, the investigated RANS turbulence models are: k-ω STD, k-ω BSL, k-ω SST and stress-ω RSM. For all ω-based turbulence models, which can be integrated through the entire viscous sub-layer, wall treatment is identical as well as y^+-insensitive. Therefore, and since the applied mesh satisfies the $y^+ \leq 1$ condition for all operating conditions, no turbulent wall functions are applied at any point.

For a qualitative comparison between experimental measurements and numerical results the spatial distribution of hydroxyl chemiluminescence is employed. As the applied observation technique does not directly quantify the OH* concentration, its numerical counterpart is normalized to facilitate an effective validation. Since averaged optical measurements merely capture a projection of the planar axisymmetric OH* distribution, an inverse Abel transformation is applied to reconstruct the unprojected data. Due to inevitable constraints in the experimental setup, the field of view solely depicts the flame's tip for some of the featured operating conditions. This unfortunately renders an inverse Abel transformation obsolete. For these cases numerical results are compared directly to averaged but otherwise unaltered chemiluminescence measurements.
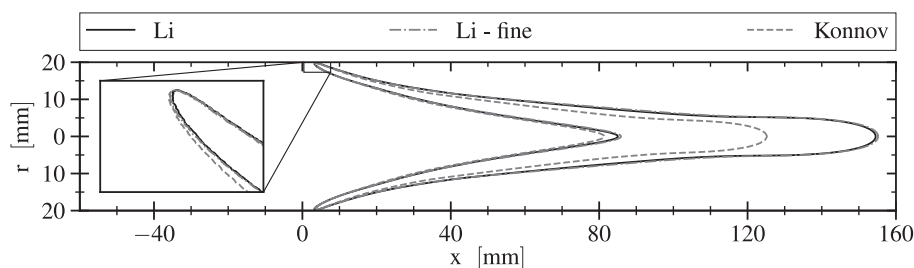
impact of different reaction mechanisms on the more realistic two dimensional flame shape and anchoring position is reviewed. For that purpose the selected mechanism by Li is compared to the more complex Konnov kinetics. Fig. 8 shows a shortened flame length for the Konnov mechanism while anchoring position and reaction zone thickness are not significantly affected. Therefore, the higher flame speed

Fig. 8 − Influence of grid resolution and kinetic mechanism on reaction front shape and anchoring position. The chemical kinetics with the least (Li) and highest (Konnov) amount of reactions are compared. Applied boundary conditions reflect case 1 while the k-ω BSL turbulence model is employed. Isolines replicate one percent of the reaction's maximum heat production.
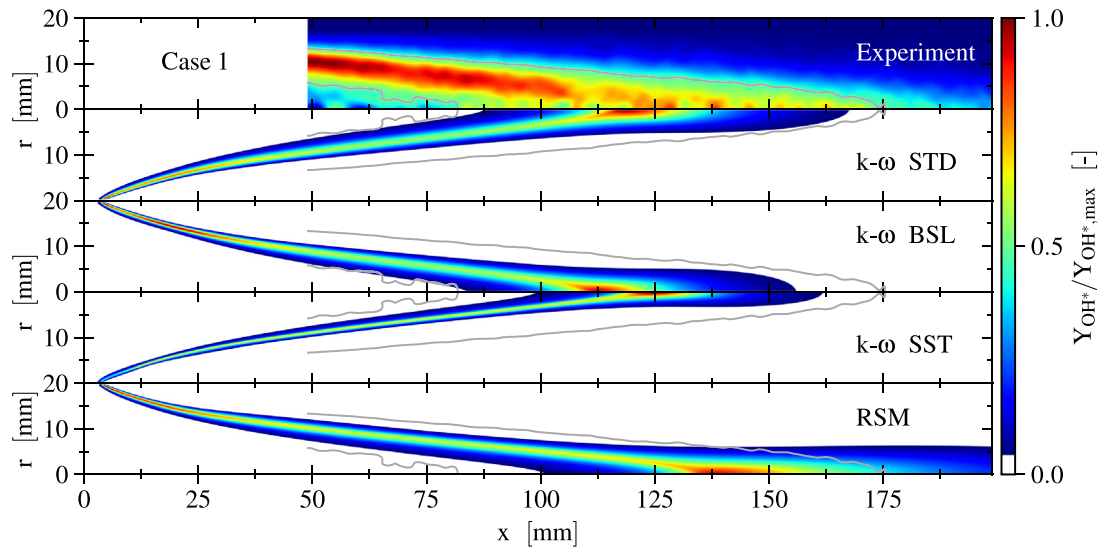
Fig. 9 — Influence of ω-based RANS turbulence models on normalized hydroxyl chemiluminescence distribution. Applied boundary conditions reflect case 1. Experimental results are visualized by inverse Abel transformation. Grey isolines correspond to values of 0.5 in the experimental measurements and are identical in all subplots. Numerical mass fractions below five percent are not shown for clarity.

Experimental results after Abel-inverse transformation and equivalent simulation outcomes featuring the introduced turbulence models are displayed in Fig. 9. Its first two contour plots show that the general flame shape is reproduced by the numerical calculations, which are obtained by the k-ω STD turbulence model. Furthermore, the total flame length coincides within satisfactory agreement. Though the flame anchoring position is not observable in the experiment, it behaves as expected and discussed in section Flame structure and wall anchoring phenomenon. Flame front thickness on the other hand exhibits some more pronounced deviation as the numerical reaction zone width is considerably smaller than the measured one.

Although general agreement in terms of overall flame shape is demonstrated for all employed turbulence models, there are some discernible differences. These are strongly pronounced for total flame length as well as reaction zone thickness. Whereas all other turbulence models predict a

highly similar flame length, the Reynolds stress model computes a severely prolonged flame as well as elongated tip form. Moreover, results by the k-ω SST model are characterized by a particularly thin reaction front while the remaining turbulence models collectively predict an almost identical flame thickness. The flame anchoring position in all applied turbulence models is profoundly alike. This is visualized in detail in Fig. 10 by depiction of the total surface heat flux over the heated wall segment. It shows that there is only a minor discrepancy between k-ω STD, k-ω BSL and RSM model while the k-ω SST model differs slightly more. Another distinct dissimilarity concerns the location of the maximum concentration of the OH* radical. Except for the k-ω SST model, the employed turbulence models predict the maximum to be at the flame anchoring position. In contrast, the k-ω SST model computes the maximum location to be at the flame tip and thus symmetry line. Furthermore, the later model predicts divergent maximum values of intermediate species. This
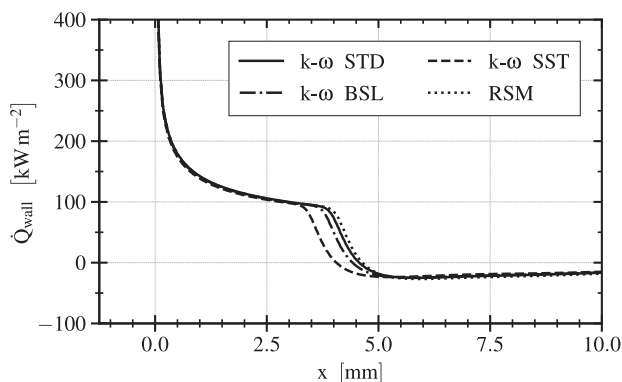

Fig. 10 — Influence of ω-based RANS turbulence models on total surface heat flux distribution along the heated wall segment. Applied boundary conditions reflect case 1. The strongest deviation is visible for the k-ω SST model.
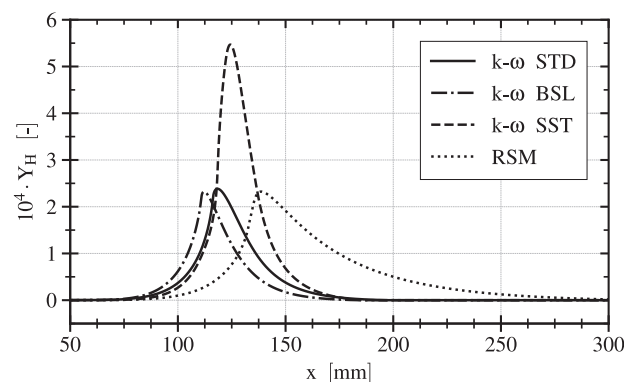

Fig. 11 — Influence of ω-based RANS turbulence models on hydrogen atom concentration along the flame's symmetry line. Applied boundary conditions reflect case 1. The strongest deviation is visible for the k-ω SST model.
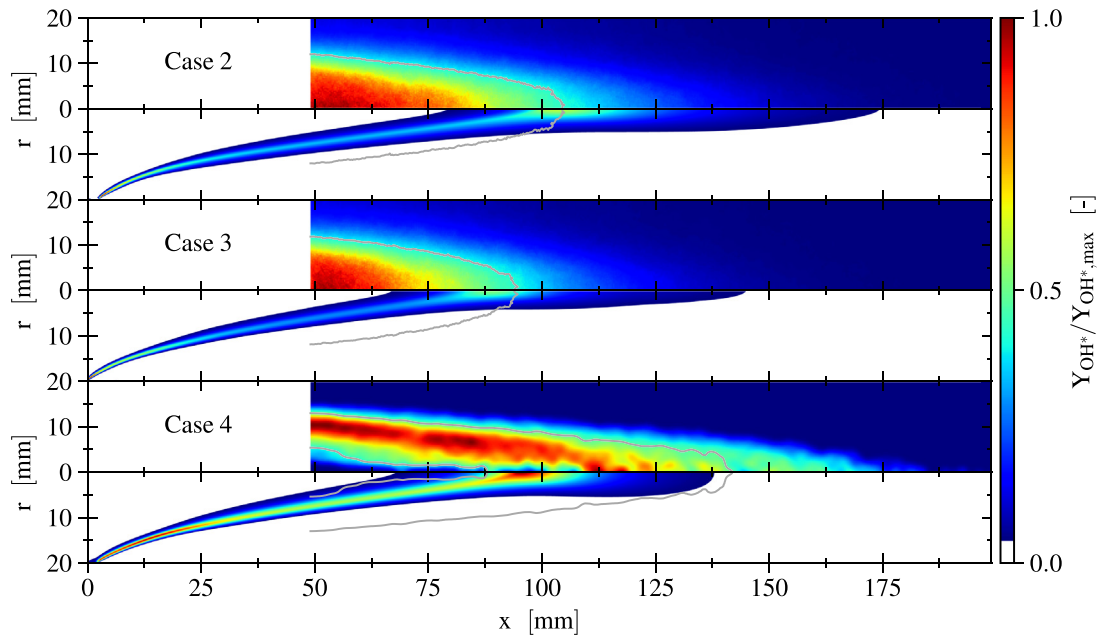
Fig. 12 – Influence of equivalence ratio (case 2) and bulk Reynolds number (case 3, case 4) on normalized hydroxyl chemiluminescence distribution. Experimental results are visualized by symmetrical averaging (case 1, case 2) or, if possible, inverse Abel transformation (case 4). Grey isolines correspond to values of 0.5 in the experimental measurements. Numerical mass fractions below five percent are not shown for clarity.
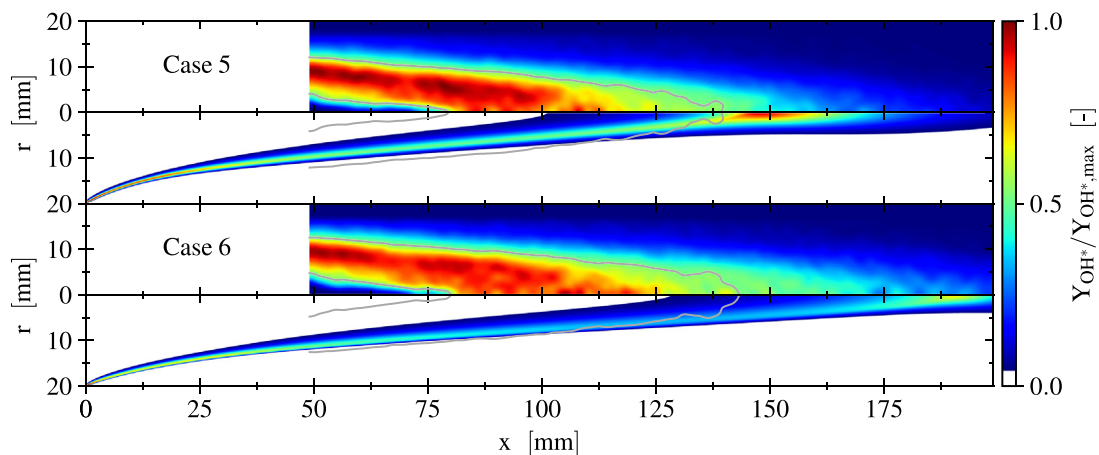

Fig. 13 – Influence of reduced unburnt mixture temperature on normalized hydroxyl chemiluminescence distribution. Experimental results are visualized by inverse Abel transformation. Grey isolines correspond to values of 0.5 in the experimental measurements. Numerical mass fractions below five percent are not shown for clarity.

behavior is visualized by the distribution of the hydrogen atom mass fraction along the axis of symmetry (Fig. 11).

Due to the minor deviations displayed by the RSM and k-ω SST model, the k-ω BSL model is selected for all subsequent simulations during the experimental validation. It should be noted that the k-ω STD model is considered to perform equally well.

Experimental validation

Besides the already assessed aspects of case 1, the numerical setup is further validated by comparison of numerical results and experimental measurements for the remaining operating conditions. Again, chemiluminescence of the OH* radical is utilized to correlate measurements and calculations. Featured operating points are summarized in Table 1. These are selected to investigate the influence of three main quantities: equivalence ratio, bulk Reynolds number and unburnt mixture temperature. A special focus is put on the universal applicability of the EDC modeling constants.

Experimental and corresponding numerical results are shown in Fig. 12 and Fig. 13. First and foremost, the implemented numerical setup is able to reproduce steady flame anchoring at externally heated walls successfully for all cases. Furthermore, the general flame shape is reproduced in each

configuration while definite deviations in flame length are only visible when the unburnt mixture temperature is significantly decreased (cases 5 and 6). The already assessed discrepancies in flame thickness are universally prevalent and pronounced about equally. Possible causes for the deviation are distinct unsteady flame oscillations in the experiment as well as neglected flame-acoustics interaction. The reaction zone could also appear thickened in the experiments because of the camera's long exposure time during measurements.

Fig. 12 visualizes the impact of differences in equivalence ratio as well as in bulk Reynolds number. Due to the acknowledged lack of Abel-inverse transformed experimental data for some of the cases, solely the reaction zone's end is depicted by the displayed isolines in these configurations, which are usually associated to abbreviated flame lengths. By increasing the inlet hydrogen mass fraction, the equivalence ratio is adjusted from $\Phi = 0.2$ (case 1) to $\Phi = 0.3$ (case 2). This induces an enhanced flame speed which results in a shortened flame length. The effect is visualized for an inlet air mass flow rate of 80 kg/h (case 2) and 60 kg/h (case 3 and case 4). A diminished total flame length is evident in both configurations. Qualitative agreement between experiments and numerical results is apparent in Fig. 12 while the EDC modeling parameters remain unaltered ($C_\gamma = 3.0$ and $C_\tau = 0.4082$).

Finally, results for operating conditions reflecting case 5 and case 6 are discussed. These illustrate the influence of colder unburnt gas mixture temperatures. The reduction of inflow enthalpy results in a much lower turbulent flame speed and thus strongly elongated flames. This behavior is evident in both experiment and numerical simulation (Fig. 13). In contrast to the previously discussed operating conditions, the simulations predict a longer flame front than observed in related experiments. This can be remedied by slight modification of EDC modeling constants. For example, decreasing C_τ or further enhancing C_γ causes a shortened flame length and can lead to improved agreement between experiment and simulation.

Conclusions

A thermal flame holder design suitable for continuous combustion devices was explored by experimental and numerical analysis. Its application to premixed hydrogen/air flames at elevated Reynolds numbers was evaluated and its performance capabilities at a diverse set of operating conditions assessed. Concluding remarks are listed in the following.

1. Calculations of a one-dimensional canonical problem showed that applying various detailed hydrogen/air kinetics does not result in significantly different outcomes. In contrast, a reduced chemical mechanism exhibited more pronounced deviations and is considered unsuitable in the presented configuration.
2. Of the applied RANS-based turbulence models the k-ω STD and k-ω BSL models perform comparably well while noticeable discrepancies, primarily concerning flame thickness, emerge for the k-ω SST model.

3. An adaptation of the EDC combustion model parameter C_γ to $C_\gamma = 3.0$ provides superior agreement between simulation and experiment. This remains valid for various inlet mass flow rates their respective bulk Reynolds numbers and imprinted equivalence ratios. But, the applicability of the altered EDC coefficients is constrained when the unburnt mixture's temperature is significantly reduced. These operating conditions, which induce an extensively elongated flame, require further calibration of the EDC modeling parameters.
4. Altogether, the stability of the flame holder design was approved during the test campaign and a validated numerical method was successfully established. Therefore, the authors are confident to apply the concept to pilot flames in future dual-fuel nanoparticle production burners using flame spray pyrolysis.

Declaration of competing interest

The authors declare that they have no known competing financial interests or personal relationships that could have appeared to influence the work reported in this paper.

Acknowledgements

REFERENCES

[1] Wan J, Zhao H. Anchoring mechanisms of methane/air premixed flame in a mesoscale diverging combustor with cylindrical flame holder. Fuel 2018;232:591−9. https://doi.org/10.1016/j.fuel.2018.06.027.
[2] Fureby C. Large eddy simulation of combustion instabilities in a jet engine afterburner model. Combust Sci Technol 2000;161:213−43. https://doi.org/10.1080/00102200008935818.
[3] Gruber MR, Baurle RA, Mathur T, Hsu KY. Fundamental studies of cavity-based flameholder concepts for supersonic combustors. J Propul Power 2001;17:146−53. https://doi.org/10.2514/2.5720.
[4] Ben-Yakar A, Hanson RK. Cavity flame-holders for ignition and flame stabilization in scramjets: an overview. J Propul Power 2001;17:869−77. https://doi.org/10.2514/2.5818.
[5] Wan J, Fan A, Yao H, Liu W. Flame-anchoring mechanisms of a micro cavity-combustor for premixed H2/air flame. Chem Eng J 2015;275:17−26. https://doi.org/10.1016/j.cej.2015.04.011.
[6] Yang W, Xiang Y, Fan A, Yao H. Effect of the cavity depth on the combustion efficiency of lean H2/air flames in a micro combustor with dual cavities. Int J Hydrogen Energy 2017;42(20):14312−20. https://doi.org/10.1016/j.ijhydene.2017.03.235.

[7] Kedia KS, Ghoniem AF. The anchoring mechanism of a bluff-body stabilized laminar premixed flame. Combust Flame 2014;161:2327–39. https://doi.org/10.1016/j.combustflame.2014.02.005.

[8] Yilmaz H. Investigation of combustion and emission performance of a micro combustor: effects of bluff body insertion and oxygen enriched combustion conditions. Int J Hydrogen Energy 2019;44(47):25985–99. https://doi.org/10.1016/j.ijhydene.2019.08.045.

[9] Huang Y, Yang V. Dynamics and stability of lean-premixed swirl-stabilized combustion. Prog Energy Combust Sci 2009;35(4):293–364. https://doi.org/10.1016/j.pecs.2009.01.002.

[10] Brouillette M, Picard M, Rancourt D, Plante J-S. Shock-induced combustion and its applications to power and thrust generation. In: 30th international symposium on shock waves, 1; 2017. p. 53–8. https://doi.org/10.1007/978-3-319-46213-4_8.

[11] Goertz V, Korp D, Al-Hasan N, Giglmaier M, Nirschl H. Experimental study of gas-dynamically induced nanoparticle synthesis by use of adapted sampling probes. Chem Eng Process: Process Intensification 2011;50:836–45. https://doi.org/10.1016/j.cep.2011.05.007.

[12] Giglmaier M. Flow physics of the gasdynamically induced particle production. Ph.D. thesis. Technical University of Munich; 2013.

[13] Dunnmon J, Sobhani S, Wu M, Fahrig R, Ihme M. An investigation of internal flame structure in porous media combustion via X-ray computed tomography. In: Proceedings of the combustion institute, 36; 2017. p. 4399–408. https://doi.org/10.1016/j.proci.2016.06.188.

[14] Sánchez-Sanz M, Fernández-Galisteo D, Kurdyumov VN. Effect of the equivalence ratio, Damköhler number, Lewis number and heat release on the stability of laminar premixed flames in microchannels. Combust Flame 2014;161:1282–93. https://doi.org/10.1016/j.combustflame.2013.11.015.

[15] Maruta K, Kataoka T, Kim NI, Minaev S, Fursenko R. Characteristics of combustion in a narrow channel with a temperature gradient. In: Proceedings of the combustion institute, 30; 2005. p. 2429–36. https://doi.org/10.1016/j.proci.2004.08.245.

[16] Bioche K, Ribert G, Vervisch L. Simulating upstream flame propagation in a narrow channel after wall preheating: flame analysis and chemistry reduction strategy. Combust Flame 2019;200:219–31. https://doi.org/10.1016/j.combustflame.2018.11.028.

[17] Zuo W, Li J, Zhang Y, Li Q, Jia S, He Z. Multi-factor impact mechanism on combustion efficiency of a hydrogen-fueled micro-cylindrical combustor. Int J Hydrogen Energy 2020;45(3):2319–30. https://doi.org/10.1016/j.ijhydene.2019.11.012.

[18] Ni S, Zhao D, Sun Y, E J. Numerical and entropy studies of hydrogen-fuelled micro-combustors with different geometric shaped rips. Int J Hydrogen Energy 2019;44(14):7692–705. https://doi.org/10.1016/j.ijhydene.2019.01.136.

[19] Zuo W, Zhang Y, Li J, Li Q, He Z. A modified micro reactor fueled with hydrogen for reducing entropy generation. Int J Hydrogen Energy 2019;44(51):27984–94. https://doi.org/10.1016/j.ijhydene.2019.09.009.

[20] Wang M, Li P, Wang F. Dependence of the blowout limit on flow structure, heat transfer, and pressure loss in a bluff-body micro-combustor. Int J Hydrogen Energy 2020;45(38):19912–25. https://doi.org/10.1016/j.ijhydene.2020.04.113.

[21] Kotani Y, Takeno T. An experimental study on stability and combustion characteristics of an excess enthalpy flame. Proc Combust Inst 1982;19:1503–9. https://doi.org/10.1016/S0082-0784(82)80327-5.

[22] Peters N. The turbulent burning velocity for large-scale and small-scale turbulence. J Fluid Mech 1999;384:107–32. https://doi.org/10.3390/en11071902.

[23] Poinsot T, Veynante D. Theoretical and numerical combustion. 2nd ed. R.T. Edwards, Inc.; 2005.

[24] Ansys fluent, 2019 R3, help system, theory guide, ANSYS, Inc.

[25] Leonhard BP. A stable and accurate convective modelling procedure based on quadratic upstream interpolation. Comput Methods Appl Mech Eng 1979;19:59–98. https://doi.org/10.1016/0045-7825(79)90034-3.

[26] Pope SS. Turbulent flows. 1st ed. Cambridge University Press; 2000.

[27] Menter FR. Two-equation eddy-viscosity turbulence models for engineering applications. AIAA J 1994;32:1598–605. https://doi.org/10.2514/3.12149.

[28] Menter FR. Review of the shear-stress transport turbulence model experience from an industrial perspective. Int J Comput Fluid Dynam 2009;23:305–16. https://doi.org/10.1080/10618560902773387.

[29] Bioche K, Pieyre A, Ribert G, Richecoeur F, Vervisch L. The role of gravity in the asymmetry of flames in narrow combustion chambers. Combust Flame 2019;203:238–46. https://doi.org/10.1016/j.combustflame.2019.02.020.

[30] Kee RJ, Rupley FM, Meeks E, Miller JA. CHEMKIN III: A FORTRAN chemical kinetics package for the analysis of gas-phase chemical and plasma kinetics. Sandia National Laboratories; 1996. Report SAND-96-8216.

[31] Bruno C, Sankaran V, Kolla H, Chen JH. Impact of multi-component diffusion in turbulent combustion using direct numerical simulations. Combust Flame 2015;162:4313–30. https://doi.org/10.1016/j.combustflame.2015.07.013.

[32] Bisetti F, Chen J-Y, Chen JH, Hawkes E. Characterization of differential diffusion effects during the constant volume ignition of a temperature stratified lean premixed hydrogen/air mixture subject to decaying turbulence. Livermore, CA: Sandia National Laboratories; 2007. Fall meeting of the western states section of the combustion institute.

[33] Magnussen BF. On the structure of turbulence and a generalized eddy dissipation concept for chemical reaction in turbulent flow. In: 19th aerospace sciences meeting, St.Louis, Missouri; 1981. https://doi.org/10.2514/6.1981-42.

[34] Magnussen BF. Modeling of NOx and soot formation by the eddy dissipation concept. Amsterdam, Holland. In: International flame research association first topic oriented technical meeting; 1989.

[35] Gran IR, Magnussen BF. A numerical study of a bluff-body stabilized diffusion flame. Part 2. Influence of combustion modeling and finite-rate chemistry. Combust Sci Technol 1996;119:191–217. https://doi.org/10.1080/00102209608951999.

[36] Bösenhofer M, Wartha E-M, Jordan C, Harasek M. The eddy dissipation concept - analysis of different fine structure treatments for classical combustion. Energies 2018;11. https://doi.org/10.3390/en11071902.

[37] Erstesvag IS, Magnussen BF. The eddy dissipation turbulence energy cascade model. Combust Sci Technol 2000;159:213–35. https://doi.org/10.1080/00102200008935784.

[38] Myhrvold T. Combustion modeling in turbulent boundary layer flows. Ph.D. thesis. Norwegian University of Science and Technology; 2003.

[39] A. De, E. Oldenhof, P. Sathiah, D. Roekaerts, Numerical simulation of Delft-jet-in-hot-coflow (DJHC) flames using the eddy dissipation concept model for turbulence-chemistry interaction, Flow, Turbul Combust 87 537–567.

[40] Wang F, Li P, Mi J, Wang J, Xu M. Chemical kinetic effect of hydrogen addition on ethylene jet flames in a hot and diluted coflow. Int J Hydrogen Energy 2015;40(46):16634–48. https://doi.org/10.1016/j.ijhydene.2015.09.047.

[41] Evans M, Medwell P, Tian Z. Modeling lifted jet flames in a heated coflow using an optimized eddy dissipation concept model. Combust Sci Technol 2015;187(7):1093–109. https://doi.org/10.1080/00102202.2014.1002836.

[42] Cam O, Yilmaz H, Tangoz S, Yilmaz I. A numerical study on combustion and emission characteristics of premixed hydrogen air flames. Int J Hydrogen Energy 2017;42(40):25801–11. https://doi.org/10.1016/j.ijhydene.2017.07.017.

[43] Jiang X, Li P, Guo J, Hu F, Wang F, Mi J, Liu Z. Detailed investigation of NO mechanism in non-premixed oxy-fuel jet flames with CH4/H2 fuel blends. Int J Hydrogen Energy 2018;43(17):8534–57. https://doi.org/10.1016/j.ijhydene.2018.03.100.

[44] Liu B, He G-Q, Qin F, An J, Wang S, Shi L. Investigation of influence of detailed chemical kinetics mechanisms for hydrogen on supersonic combustion using large eddy simulation. Int J Hydrogen Energy 2019;44:5007–19. https://doi.org/10.1016/j.ijhydene.2019.01.005.

[45] Vincent-Randonnier A, Sabelnikov V, Ristori A, Zettervall N, Fureby C. An experimental and computational study of hydrogen-air combustion in the LAPCAT II supersonic combustor. In: Proceedings of the combustion institute, 37; 2019. p. 3703–11. https://doi.org/10.1016/j.proci.2018.05.127.

[46] Kumar PP, Kim K-S, Oh S, Choi J-Y. Numerical comparison of hydrogen-air reaction mechanisms for unsteady shock-induced combustion applications. J Mech Sci Technol 2015;29:893–8. https://doi.org/10.1007/s12206-015-0202-2.

[47] Alekseev VA, Christensen M, Konnov AA. The effect of temperature on the adiabatic burning velocities of diluted hydrogen flames: a kinetic study using an updated mechanism. Combust Flame 2015;162:1884–98. https://doi.org/10.1016/j.combustflame.2014.12.009.

[48] Li J, Zhao Z, Kazakov A, Dryer FL. An updated comprehensive kinetic model of hydrogen combustion. Int J Chem Kinet 2004;36:566–75. https://doi.org/10.1002/kin.20026.

[49] Chemical-Kinetic mechanisms for combustion applications, San Diego Mechanism web page, Mechanical and Aerospace Engineering, University of California at San Diego.

[50] Davis SG, Joshi AV, Wang H, Egolfopoulos F. An optimized kinetic model of H2/CO combustion. Proc Combust Inst 2005;30:1283–92. https://doi.org/10.1016/j.proci.2004.08.252.

[51] P. Boivin, Reduced-kinetic mechanism for hydrogen and syngas combustion including autoignition, Ph.D. thesis, Universidad Carlos III, Madrid.

[52] Kathrotia T, Fikri M, Bozkurt M, Hartmann M, Riedel U, Schulz C. Study of the H+O+M reaction forming OH kinetics of OH* chemiluminescence in hydrogen combustion systems. Combust Flame 2010;157:1261–73. https://doi.org/10.1016/j.combustflame.2010.04.003.

[53] Goodwin DG, Speth RL, Moffat HK, Weber BW. Cantera: an object-oriented software toolkit for chemical kinetics, thermodynamics, and transport processes. 2018. https://doi.org/10.5281/zenodo.1174508., 2.4.0. https://www.cantera.org.

[54] Aung KT, Hassan MI, Faeth GM. Flame stretch interactions of laminar premixed hydrogen/air flames at normal temperature and pressure. Combust Flame 1997;109:1–24. https://doi.org/10.1016/S0010-2180(96)00151-4.

[55] Huang Z, Zhang Y, Zeng K, Liu B, Wang Q, Jiang D. Measurements of laminar burning velocities for natural gas-hydrogen-air mixtures. Combust Flame 2006;146:302–11. https://doi.org/10.1016/j.combustflame.2006.03.003.

[56] Ilbas M, Crayford AP, Yilmaz I, Bowen PJ, Syred N. Laminar-burning velocities of hydrogen-air and hydrogen-methane-air mixtures: an experimental study. Int J Hydrogen Energy 2006;31:1768–79. https://doi.org/10.1016/j.ijhydene.2005.12.007.

[57] Dong C, Zhou Q, Zhao Q, Zhang Y, Xu T, Hui S. Experimental study on the laminar flame speed of hydrogen/carbon monoxide/air mixtures. Fuel 2009;88:1858–63. https://doi.org/10.1016/j.fuel.2009.04.024.

[58] Proch F, Kempf AM. Modeling heat loss effects in the large eddy simulation of a model gas turbine combustor with premixed flamelet generated manifolds. In: Proceedings of the combustion institute, 35; 2015. p. 3337–45. https://doi.org/10.1016/j.proci.2014.07.036.